Journal of Materials Chemistry C

Accepted Manuscript

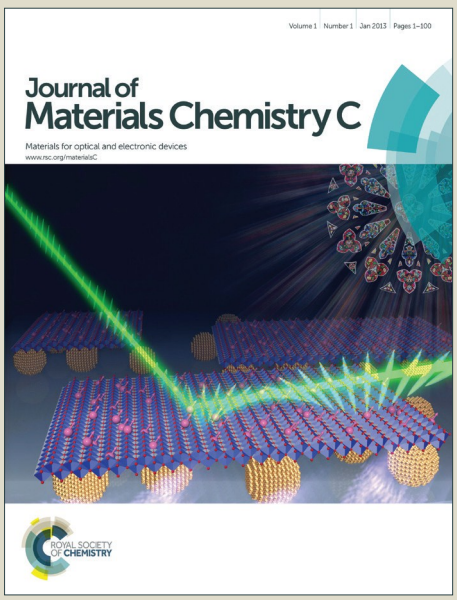

ROYAL SOCIETY OF CHEMISTRY

www.rsc.org/materialsC

Journal of
Materials Chemistry C

RSC Publishing

PAPER

High temperature stability dielectric properties of $(K_{0.5}Na_{0.5})_{0.985}Bi_{0.015}Nb_{0.99}Cu_{0.01}O_3$ ceramics with core-shell microstructures

Cite this: DOI: 10.1039/x0xx00000x

Zhiyong Liu, Huiqing Fan* and Mengmeng Li

Received XX th XX 2015,
Accepted XX th XX 2015

DOI: 10.1039/x0xx00000x

www.rsc.org/

New high temperature ceramic capacitors $(K_{0.5}Na_{0.5})_{(1-x)}Bi_xNb_{(1-2x/3)}Cu_{2x/3}O_3$ (x = 0−0.03) with Bi substitution for A site and Cu substitution for B site were synthesized using a solid state reaction process. Owning to its inhomogeneous microstructure and diffuse phase transition, $(K_{0.5}Na_{0.5})_{0.985}Bi_{0.015}Nb_{0.99}Cu_{0.01}O_3$ shows a stable permittivity near 1350 at a broad temperature range (40 °C–520 °C) and the capacitance variation is maintained smaller than ±15%, thereby paving the way for achieving high temperature capacitors in KNN based materials. Furthermore, the grain and grain boundary contribution to the capacitance have been separated using impedance spectroscopy, the grain boundary effects have temperature independent capacitance, whereas grain effects show a capacitance maximum at the tetragonal to cubic phase transition.

Introduction

High temperature ceramic capacitors are being developed and widely used in many fields, such as automotive vehicles, military equipments, geothermal, space exploration, and so on.[1-5] Traditional high temperature capacitors based on $BaTiO_3$ are specified to upper working temperatures of 125 °C, 150 °C, and 175 °C for X7R, X8R, and X9R, respectively.[4-6] However, an increase in conductivity at high temperature and a sharp decrease in permittivity at >200 °C effectively limits the usefulness of these materials at elevated temperatures. Therefore, new materials with a large dielectric permittivity, low permittivity variation and low dielectric loss in a broad temperature range is urgent for high temperature capacitors application.

Currently, a number of perovskite lead-free dielectrics with near-stable relative permittivity at temperature above 200 °C have been reported. These include: $BaTiO_3$–$Bi(Zn_{1/2}Ti_{1/2})O_3$–$BiScO_3$,[2] $(Ba_{0.8}Ca_{0.2})TiO_3$–$Bi(Mg_{0.5}Ti_{0.5})O_3$–$NaNbO_3$,[3] $BaTiO_3$–$Bi(Mg_{0.5}Zr_{0.5})O_3$,[7] $Ba_{0.8}Ca_{0.2}TiO_3$–$Bi(Zn_{0.5}Ti_{0.5})O_3$,[8] $Bi_{0.5}Na_{0.5}TiO_3$–$Bi_{0.5}K_{0.5}TiO_3$–$K_{0.5}Na_{0.5}NbO_3$,[9] $Bi_{0.5}Na_{0.5}TiO_3$–$BaTiO_3$–$K_{0.5}Na_{0.5}NbO_3$[10] and $Bi_{0.5}Na_{0.5}TiO_3$–$BaTiO_3$–$CaZrO_3$.[11] However, compared with $BaTiO_3$ and $Bi_{0.5}Na_{0.5}TiO_3$ based materials, the reports on temperature stable dielectric properties of $(K_{0.5}Na_{0.5})NbO_3$ based materials are rare.[12,13] $K_{0.5}Na_{0.5}NbO_3$ as the candidates for lead-free piezoelectric materials has been studied extensively,[14-20] The un-doped $(K_{0.5}Na_{0.5})NbO_3$ ceramics exhibits two phase transitions: one from orthorhombic to tetragonal at ~200 °C (T_{O-T}) and another from tetragonal to cubic phase at ~420 °C (T_C). Just like $Bi_{0.5}Na_{0.5}TiO_3$ based temperature stable dielectrics,[10,11] $(K_{0.5}Na_{0.5})NbO_3$ also can be modified with different ions or the formation of solid solutions with other ferroelectrics, induce the diffuse phase transitions in a broad temperature range, which makes the $(K_{0.5}Na_{0.5})NbO_3$ based ceramics promising candidates for high temperature capacitors materials.

CuO as sintering aid or dopant in KNN system obviously promote densification, reduce abnormal grain growth thus giving a uniform grain sizes. A mildly decrease of T_C and T_{O-T} phase transition temperatures also obtained in the CuO doped KNN system.[21,22] Bi_2O_3 as dopant can introduce diffuse phase transition, result a broader dielectric spectroscopy in KNN ceramic.[23,24] In this study, we synthesized $(K_{0.5}Na_{0.5})_{(1-x)}Bi_xNb_{(1-2x/3)}Cu_{2x/3}O_3$ ceramics with Bi substitution for A site and Cu substitution for B site, expected to obtain a high temperature stability dielectric property. The dielectric permittivity contribution from grain and grain boundary have been separated by using impedance spectroscopy at elevate temperature.

Experimental procedure

Polycrystalline ceramics $(K_{0.5}Na_{0.5})_{(1-x)}Bi_xNb_{(1-2x/3)}Cu_{2x/3}O_3$ (x = 0, 0.005, 0.01, 0.015, 0.02, 0.03, abbreviated as KNN–xBC) were prepared by a solid state reaction process. Stoichiometric

raw oxides of K_2CO_3, Na_2CO_3, Nb_2O_5, CuO, and Bi_2O_3 (Sinopharm Chemical Reagent Co., Ltd, CN) were mixed and then milled using zirconia ball media with ethanol for 12 h. After ball milling, the mixtures were dried and then calcined at 850 °C for 2 h. The precursor powders were ball milled for 24 h again, dried and cold isostatically pressed into pellets at 300 MPa. The pressed pellets were sintered at 1070−1160 °C for 2 h dependent on their components; the pellets were surrounded by powder of the same composition to minimize volatilization losses. The obtained ceramics were grinded and polished with 5 nm diamond paste, and thermally etched (1020 °C for 30 min) for surface morphology measurements.

Density of the ceramics was measured by using the Archimedes method. Crystal structures of the ceramics were detected by using X-ray diffraction (XRD) (X'Pert PRO MPD, Philips, Eindhoven, The Netherlands) with a nickel filter (CuKα radiation) over 2θ in the range of 20−60° at room temperature, Powders for XRD analysis were obtained by crushing sintered pellets. Raman scattering experiments of the ceramics were performed with an instrument (LabRAM HR800, Horiba JobinYvon, Lyon, France) in a backward scattering geometry (the exciting source was the 514.5 nm line from an argon ion laser). The chemical bonding states of the ceramics were investigated by an X-ray photoelectron spectroscopy (XPS, Model ESCALAB250; Thermo Fisher Scientific, Waltham, MA). The thermally etched surface and new fracture morphologies of the ceramics were obtained by using a field emission scanning electron microscopy (FE−SEM) (SEM, DSM 950, Zeiss, Oberkochen, Germany) operated at 15 kV; grain size was estimated using the linear intercept method. Silver electrodes with appropriate configurations were coated on both polished surfaces and fired at 550°C for 30 min to form a metal-insulator-metal (MIM) capacitor for electrical test. Weak-field dielectric responses were measured using a precision impedance analyzer (4294A, Agilent, Santa Clara, CA) associated with a temperature controller (TP94, Linkam, Surrey, U.K.) over a temperature range of 25–520 °C at a heating rate of 3 °C/min. Dependence of the ferroelectric polarization (*P*) were measured at 10 Hz, by using a ferroelectric test unit (TF-2000, aix-ACCT, Aachen, Germany). Variable-temperature impedance spectra were performed by using an Impedance Analyzer (SI 1260, Solartron, Hampshire, U.K.); before each measurement was taken, the samples had been kept at the measurement temperature for 30 min to reach thermal equilibrium.

TEM samples were prepared via standard procedures including grinding, cutting, dimpling, and ion milling. The dimpled disks were annealed at 200 °C for 2 h to minimize artifacts introduced during mechanical thinning. Transmission electron microscopic (TEM) analyses, including TEM annular bright field (ABF) imaging, high angle annular dark field (HAADF) and energy dispersive X-ray spectroscopy (EDS) mapping, were performed using an TEM (Tecnai F30, FEI, Hillsboro, OR) at 200 kV accelerating voltage.

Results and discussion

Room temperature XRD patterns of the KNN−*x*BC ceramics are displayed in Fig. 1(a). No obvious secondary phase was found in the XRD patterns. The pure KNN is orthorhombic phase with two natural independent diffraction peaks, (202) and (020),[18] in the 2θ = 44°–47° range (Fig. 1b). Notably, with increasing BC content (*x*) gives rise to the mergence of the two peaks. For compositions with x = 0.01−0.03, the relatively integrated intensity of the (202) and (020) peak fitting by Gaussian-Lorentz function with the best fitting shown in Fig. 1b. It can be observed that the relatively integrated intensity of the (202) peak is higher than that of the (020) peak, this indicate that the crystal structure maintain orthorhombic phase. Additionally, the result of XPS analysis was Cu and Bi ions at the same oxidation state after sintering in KNN-0.015BC, detailed discussion can be found in ESI Fig. S1†. According to the principles of crystal chemistry and radius matching rule, K^+ (0.164 nm, CN = 12), Na^+ (0.139 nm, CN = 12), and Bi^{3+} (0.138 nm, CN = 12)[25] occupy the A sites of ABO_3 perovskite structure, while Nb^{5+} (0.064 nm, CN = 6), Cu^{2+} (0.073 nm, CN = 6) ions occupy the B sites. Consequently, the addition of Bi and Cu gave rise to a small shrinkage of the cell volume and thus induces the (202) peak closed to the (020) peak.

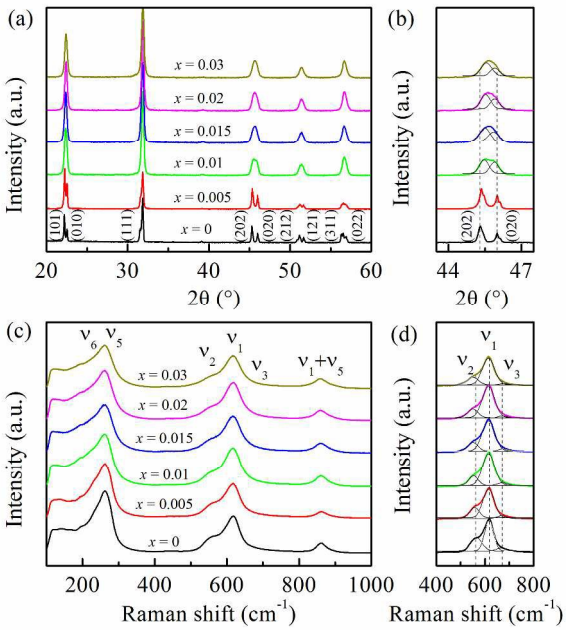

Fig. 1 XRD patterns of KNN–*x*BC ceramics at (a) 2θ = 20−60° and (b) 2θ = 44−47°, Raman spectra of KNN–*x*BC ceramics at Raman range: (c) 100-1000 cm^{-1} and (d) 400-800 cm^{-1}.

To further confirm the crystal structure, room temperature Raman spectra of KNN−*x*BC ceramics are plotted in Fig. 1c. The observed vibrations can be separated into external modes related to cations and internal modes of coordination octahedra.[26,27] Among the full Raman active mode of KNN, ν_1, ν_2, and ν_3 are stretching modes, ν_5 and ν_6 are bending modes of the NbO_6 octahedra.[26] In order to better illustrate the changes in

peak characteristics of the ceramics, spectra deconvolution was performed according to Gauss functions by means of a best fitting shows in Fig. 1d. Note that, with increasing the doping content, the two bands, v_1 and v_2 corresponding to NbO_6 bending vibration shift to the lower wave number, the v_3 band centred around 675 cm^{-1} gradually decrease with the increase of BC compositions. Owing to the different ion radius, ionicity and mass, the introduction of Bi^{3+} and Cu^{2+} cations into the lattice of KNN leads to a perturbation to the original energy levels. The peak shift to a lower frequency is due to a decrease in binding strength caused by the extending of the distance between Nb^{5+} and its coordinated oxygen. Moreover, v_3 bands near vanish with x = 0.03. It was reported that the disappearance of the band in Raman spectrum could be due to the vanishing of the tilting between the adjacent NbO_6 octahedra,[28] which suggests the ordered microstructure of the ceramics is deteriorating with increasing the BC content. Therefore, there is a loss of polarity of the ceramics (ESI Fig. S2†).

Figure 2 shows the SEM micrographs of thermal etched surface and fractured surface microstructures of KNN–xBC ceramics. The grain size is ~8 μm for the KNN and KNN–0.005BC (ESI Table S1†). However, with increasing BC content, the grain size decreased rapidly to below 1 μm. Additionally, the fracture surfaces indicate that with BC addition increasing, the ceramics density is increased (ESI Table S1†). From the results of F. Azough *et al.*[21] and X. Tan *et al.*,[22] Cu ions can effectively promote the densification, reduce the abnormal grain growth thus giving a uniform grain size of the ceramics. The decrease in grain size should be attributed to the addition of Bi ions; Bi ions may be concentrated near the grain boundaries and reduce their mobility during the sintering. As a result, the mass transportation becomes weakened and the grain growth is inhibited. The same phenomenon has also been observed in other Bi doped KNN systems.[13,23,24]

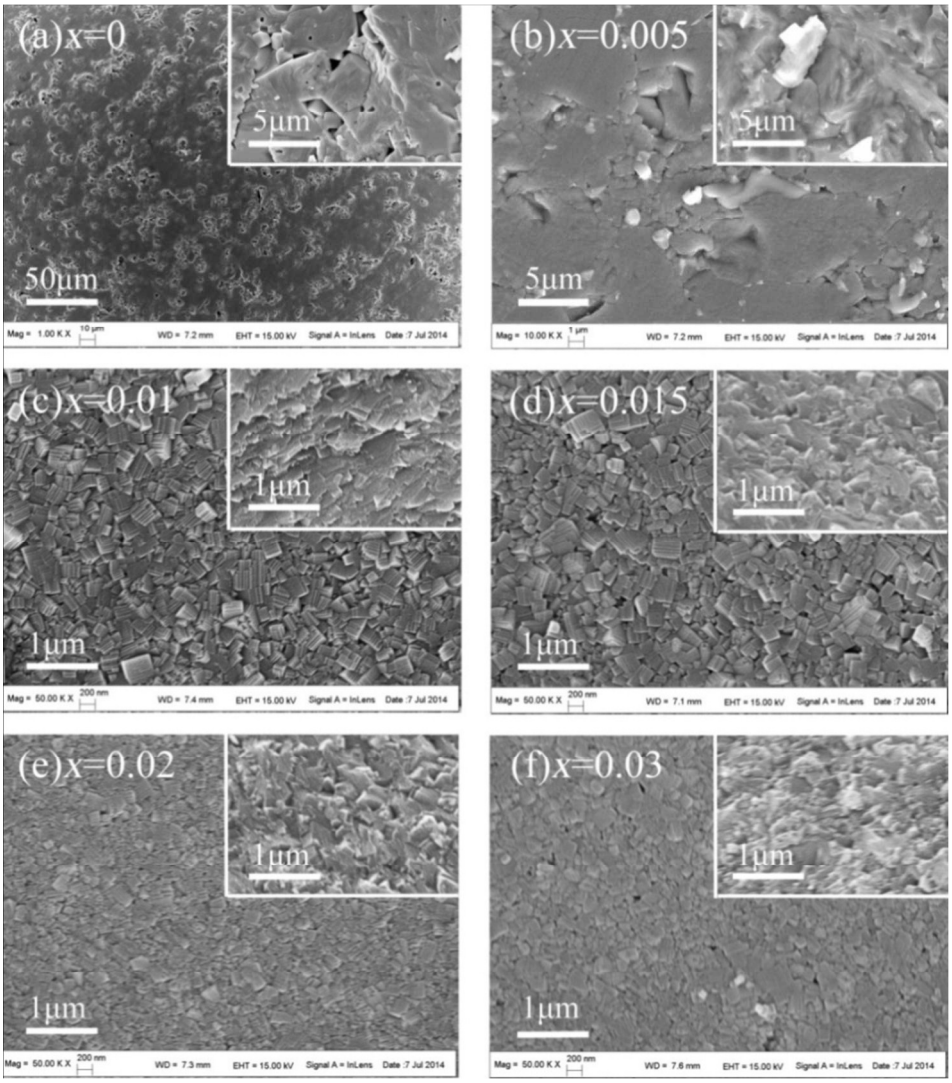

Fig. 2. SEM micrographs of thermal etching surface and fractured surface microstructures for KNN–xBC ceramics.

Temperature dependence of dielectric permittivity and dielectric loss of KNN–*x*BC ceramics at frequency of 100 kHz are shown in Fig. 3. The variations of T_C and T_{O-T} as a function of content *x* are shown in the inset of Fig. 3a, both the phase transitions temperatures of T_{O-T} and T_c are simultaneously shift to a lower temperature. Interestingly, the phase transition temperature range around T_c becomes broader with increasing the addition of BC content, which can be called diffuse phase transition (Fig.4b). The broadening of dielectric peak could be due to lattice disordering or the strain induced by the doping.[12] In addition, as the BC content increased, the dielectric permittivity around T_c of the ceramics drop rapidly. Particularly, it is worth to notice that the x = 0.015, 0.02, and 0.03 ceramics exhibit flat dielectric spectroscopy, a dielectric permittivity near 1350 over a wide temperature range for KNN-0.015BC (ESI Table S1†). Moreover, it also can be observed that dielectric loss of the ceramics is influenced by the addition of BC (Fig. 3b), the dielectric loss decreased with increasing the addition of BC content. For KNN-0.015BC, the ceramic possess a dielectric loss lower than 5% at broad temperature range (25 °C–430 °C). The reason of low dielectric loss may be the improvement of bulk density (ESI Table S1†) and loss of polarity of the ceramics (ESI Fig. S2†).

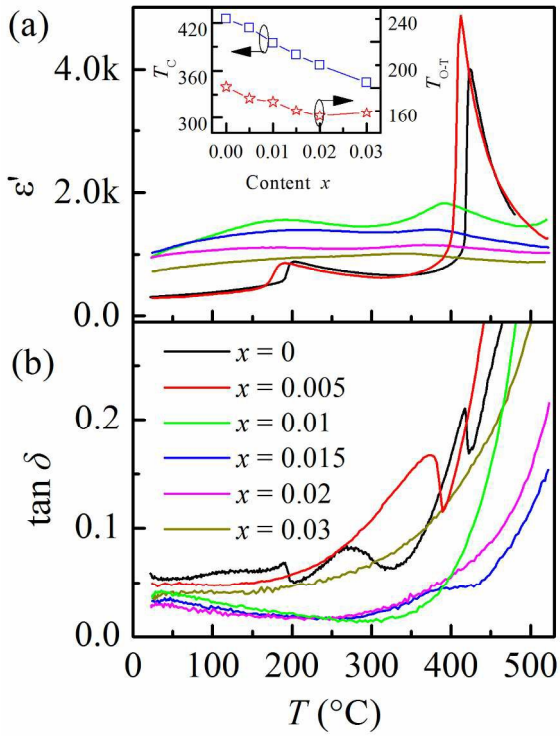

Fig. 3. Temperature dependence of (a) dielectric permittivity and (b) dielectric loss for KNN–*x*BC ceramics at 100 kHz. Insert shows T_C and T_{O-T} versus content *x*.

The most important dielectric characteristics for high temperature capacitance materials are the capacitance variation in the operation temperature range. Figure 4a shows $\Delta\varepsilon'/\varepsilon'_{150\,°C}$ ($\Delta\varepsilon'=\varepsilon'-\varepsilon'_{150\,°C}$) as a function of temperature for KNN – *x*BC ceramics at 100 kHz. It is found that the curves vary obviously with the content of BC. They reveal that BC influences significantly on the variation in capacity of KNN system. In addition, the variation in $\Delta\varepsilon'/\varepsilon'_{150\,°C}$ is ±15% for $0.015 \leqslant x \leqslant 0.03$. Especially, KNN-0.015BC exhibits stable dielectric permittivity (1350) and dielectric loss (tan δ) lower than 5% at high temperature (~430 °C). The dielectric properties of KNN–*x*BC, x = 0.015 and 0.02, are summarized and compared with a representative selection of other lead-free high temperature dielectric ceramics in Table 1. These results indicate that KNN–0.015BC ceramics is a promising candidate for high temperature ceramics capacitor.

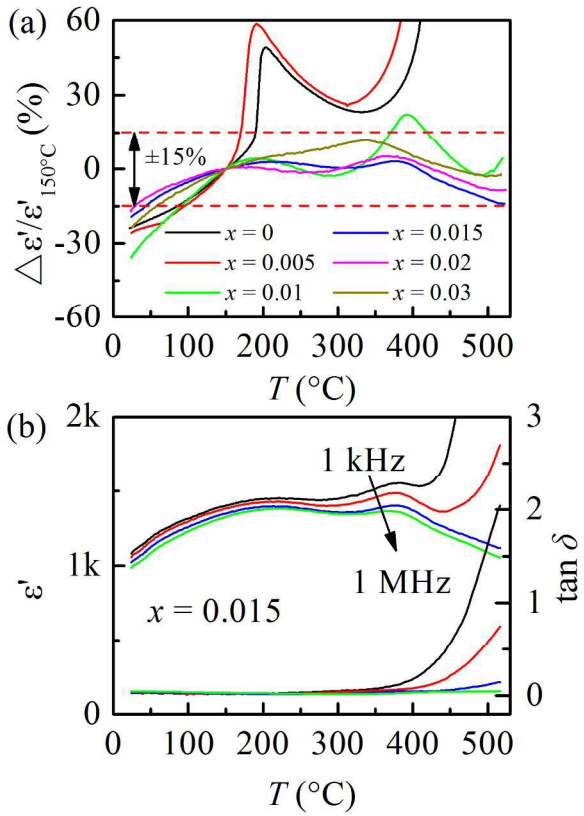

Fig. 4. (a) $\Delta\varepsilon'/\varepsilon'_{150°C}$ as a function of temperature for KNN–*x*BC ceramics, (b) Temperature dependence of dielectric permittivity and dielectric loss for KNN–0.015BC ceramics at 1 kHz, 10 kHz, 100 kHz, and 1 MHz.

In general, polycrystalline ceramics are composite with grain and grain boundary. For the doped capacitor ceramics, there are frequently show different components in grain and grain boundary, and display different dielectric responses under electro-active.[30,31] In order to distinguish between grain and grain boundary contributions to the dielectric permittivity, the

Table 1 Comparison of dielectric properties of KNN–*x*BC ceramics with other high temperature lead-free capacitor materials at 100 kHz

	T_m (°C)	ε' (150 °C)	tanδ (%) (150 °C)	Temperature range (°C) ($\Delta\varepsilon'/\varepsilon'_{150°C} < \pm 15\%$)	Ref.
KNN-0.015BC	380	1350	2.0	40-520	this work
KNN-0.02BC	367	1084	2.0	29-520	this work
BCT-BMT-0.2NN	0	600‡	2.0‡	-70-500‡	[3]
BT-0.3BMZ	20	570§	2.0	-20-430	[7]
BCT-0.3BZT	90§	1030§	1.2§	25-425	[8]
BCT-0.5BMT	120‡	800‡	2.0§	30-550§	[29]
BNT-BT-0.15KNN	250§	2349‡	2.0§	40-330§	[10]
BNT–BT–0.15CZ	320§	946‡	3.0§	52-490‡	[11]
KNN-0.075BNN	370	1250§	3.0§	50-450	[12]
0.03BZN-0.97KNN	350	2000	2.0§	100-400	[13]

BCT-BMT-0.2NN, $0.45(Ba_{0.8}Ca_{0.2})TiO_3$–$0.35Bi(Mg_{0.5}Ti_{0.5})O_3$–$NaNbO_3$; BT-0.3BMZ, $0.7BaTiO_3$–$0.3Bi(Mg_{0.5}Zr_{0.5})O_3$; BCT-0.3BZT, $0.7(Ba_{0.8}Ca_{0.2})TiO_3$–$0.3Bi(Zn_{0.5}Ti_{0.5})O_3$; BCT-0.5BMT, $0.5Ba_{0.8}Ca_{0.2}TiO_3$–$0.5Bi(Mg_{0.5}Ti_{0.5})O_3$; BNT-BT-0.15KNN, $0.85(0.94Bi_{1/2}Na_{1/2}TiO_3$–$0.06BaTiO_3)$–$0.15K_{0.5}Na_{0.5}O_3$; BNT–BT–0.15CZ, $0.85(0.94Bi_{1/2}Na_{1/2}TiO_3$–$0.06BaTiO_3)$–$0.15CaZrO_3$; KNN-0.075BNN, $0.925(K_{0.5}Na_{0.5})NbO_3$–$0.075Ba_2NaNb_5O_{15}$; 0.03BZN-0.97KNN, $0.03Bi(Zn_{2/3}Nb_{1/3})O_3$–$0.97(K_{0.5}Na_{0.5})NbO_3$.

‡ 1 kHz

§ Estimated numerical values from diagrams in reference cited.

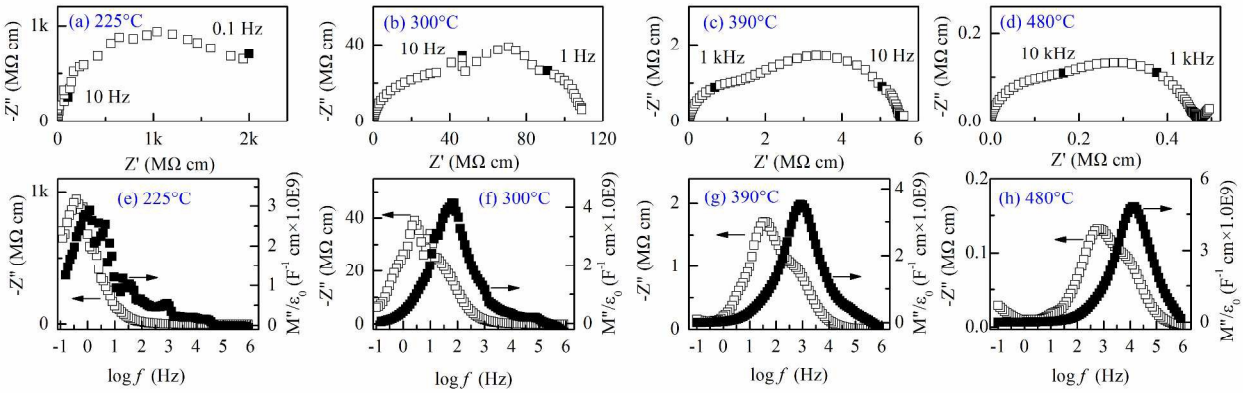

Fig. 5 Impedance complex plane plot and combined $-Z''/M''$ spectroscopic plots for KNN–0.015BC: (a) and (e) at 225°C, (b) and (f) at 300°C, (c) and (g) at 390°C, (d) and (h) at 480°C.

complex impedance spectroscopy by using analysis the KNN–0.015BC ceramic at range around the ferroelectric transition temperature are shown in Fig. 5. Typical impedance analyzed in terms of an equivalent circuit containing, ideally, two parallel RC elements connected in series is shown in the inset of Fig. 6a. To carry out a more thorough investigation of the electrical properties, corresponding Z'' and M'' spectroscopic of the impedance also plots in elevate temperatures. Commonly, the peaks of M''(f) spectra are dominated by the parts with the smallest capacitor value and usually relate to grain responses, whereas the peaks of Z''(f) spectra are dominated by those with the largest R value and are often ascription with the resistive grain boundary responses in electro-ceramics. If the maxima in M''(f) and Z''(f) spectra occur at the different frequency (f_{max}), that is, they share the dissimilar time constant, it suggests that the electro-active region of grain and grain boundary are different.[32]

From Fig. 5a, impedance data at 225 °C shows a single arc, and corresponding Z'' maxima is present at 0.5 Hz in the Z'' spectra, accompany with a high frequency flat profile in the M'' spectrum (Fig. 5e), suggesting this Z^* arc is associated with a grain effect.[33] For the data collected at 300 °C, an irregular double arc appeared in Fig.5b, and the Z'' maxima shifts to 5 Hz (Fig. 5f). Besides, another shoulder Z'' peak appears at 60 Hz in the Z'' spectra. At the same frequency, a M'' maximum appears in the M'' spectrum. It can be concluded that the high frequency arc is assigned to grain effect, whereas the low frequency arc is associated with grain boundary effect.[33] For further increase the measure temperatures, a regular double arc is observed (Fig. 5c, d), and the Z'' peak (Fig. 5f,g) belong to grain boundary be

observed shift to the high frequency. Corresponding, the M'' maxima pertain to grain also shift to the high frequency. The maxima in M''(f) and Z''(f) spectra occur at the different frequency (f_{max}) at elevate temperature, this also indicates that the grain boundary regions may be considered as grain shells that have slightly different composition to grain cores. In addition, the totally AC resistivity values ρ can be estimated by the low frequency arc intercept. The ρ value ranged from ~10^9 Ωcm at 225 °C to ~10^4 Ωcm at 480 °C.

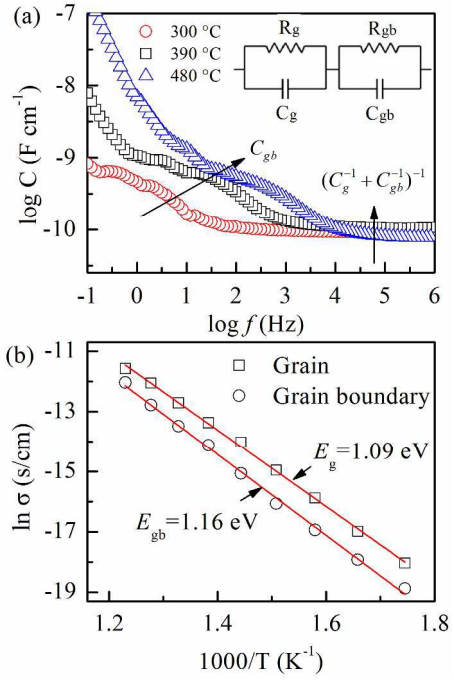

Fig. 6 (a) Capacitance spectroscopic plots at several temperatures of KNN−0.015BC ceramics, (b) Arrhenius plots of the grain and grain boundary conductivity of KNN−0.015BC ceramics.

The log C as a functional of frequency are shown in Fig. 6(a), in which capacitance data (C) obtained by re-plotting the same Z* data. The data at 300 °C shows a high frequency plateau representing a value of 0.091 nF/cm. As the temperature is increased, the peak is displaced toward higher frequency. A more steeply inclined region is observed which reaches a capacitance of 0.137 nF/cm at 1300 Hz and 480 °C. From the results obtained by Li,[34,35] the high frequency capacitance plateau is referred to grain effects (in fact, this is only approximately correct), whereas the low frequency capacitance plateau is ascribed to grain boundary effects. Corresponding, Logarithmic conductivity (300−540 °C) of the two components associated with grain and grain boundary effects obtained from the intercept of the data in their Z* (Fig. 5) plots are shown in Fig. 6b. A good linear fitting for log σ *vs* 1000/T plots at whole temperature range and the activation energy (E_a) of grain boundary is higher than grain. This suggests that they are structurally/compositionally different in the grain and grain boundary.[36]

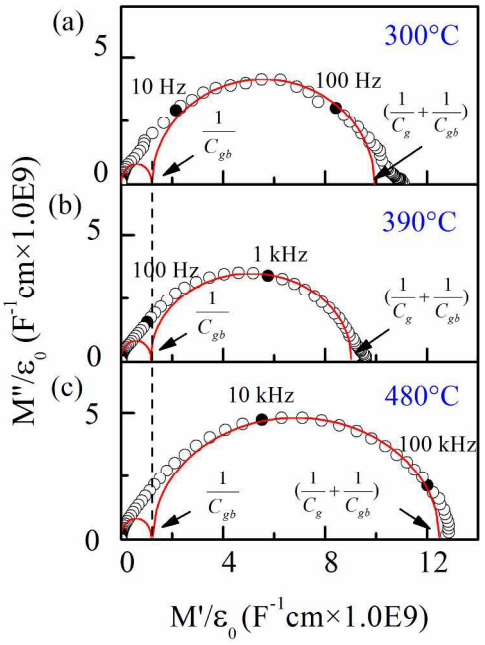

Fig. 7 Electric modulus plane complex plots at several temperatures for KNN-0.015BC ceramic, the red solid lines are fitting spectra with R_bC_b element.

For the equivalent circuit consisting of two parallel RC elements, as shown in the inset of Fig.6a, the impedance for these circuits:[36]

$$Z^* = (\frac{1}{R_g} + j\omega C_g)^{-1} + (\frac{1}{R_{gb}} + j\omega C_{gb})^{-1} \quad (1)$$

and

$$M^* = j\omega C_0 Z^* \quad (2)$$

The corresponding equation for complex electrical modulus M' and M'' are obtained by associate with Eq. (1) and (2). These are:

$$M' = \frac{C_0}{C_g}\left(\frac{(\omega R_g C_g)^2}{1+(\omega R_g C_g)^2}\right) + \frac{C_0}{C_{gb}}\left(\frac{(\omega R_{gb} C_{gb})^2}{1+(\omega R_{gb} C_{gb})^2}\right) \quad (3)$$

and

$$M'' = \frac{C_0}{C_g}\left(\frac{\omega R_g C_g}{1+(\omega R_g C_g)^2}\right) + \frac{C_0}{C_{gb}}\left(\frac{\omega R_{gb} C_{gb}}{1+(\omega R_{gb} C_{gb})^2}\right) \quad (4)$$

Combination of the electric modulus formalisms since each parallel RC element gives rise to a semicircle in the complex plane (M' vs M'') are shown in Fig. 7. The high frequency arcs of complex plane are associated with $C_g^{-1} + C_{gb}^{-1}$, whereas the low frequency intercepts are C_{gb}^{-1}. Interestingly, the intercepts associated with C_{gb}^{-1} are maintain unchanged at the temperature range of 300−480 °C, and a minimum value of $C_g^{-1} + C_{gb}^{-1}$ is

obtained at 390 °C. Fig. 8 plots the electrical permittivity of the grain boundary (ε'_{gb}) and grain (ε'_{g}) values obtained by complex *M′ vs M″* plane at elevate temperatures. It can be observed that the ε'_{gb} values are around 9500 and exhibit temperature independent, whereas the ε'_{g} *vs T* plots reveal a peak at 390 °C. Through the results obtained in Fig 4b, the ε'_{g} peak which associate with the T_c phase transition. Moreover, the whole dielectric permittivity can be calculation by the equivalent *RC* circuit $\varepsilon' \approx \varepsilon'_{g} \approx (\varepsilon_{g}^{-1} + \varepsilon_{gb}^{-1})^{-1}$, and the permittivity values are almost equal to that of obtained in Fig. 4b. These results reveal that the grain is ferroelectric and the grain boundary is non-ferroelectric, and can be distinguished from the capacitance data: the grain boundary effects have temperature independent capacitance, whereas grain effects show a capacitance maximum at the tetragonal to cubic phase transition temperature.

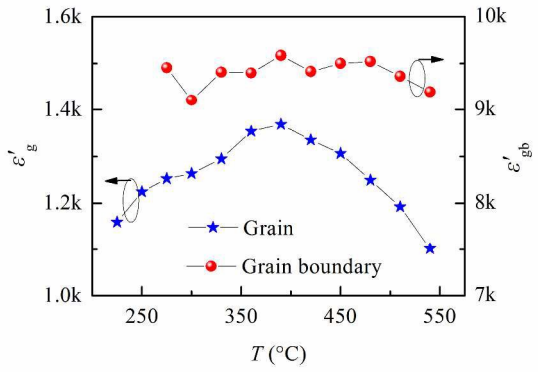

Fig. 8. Temperature dependence of the dielectric permittivity of grains and grain boundarys for KNN-0.015BC ceramics.

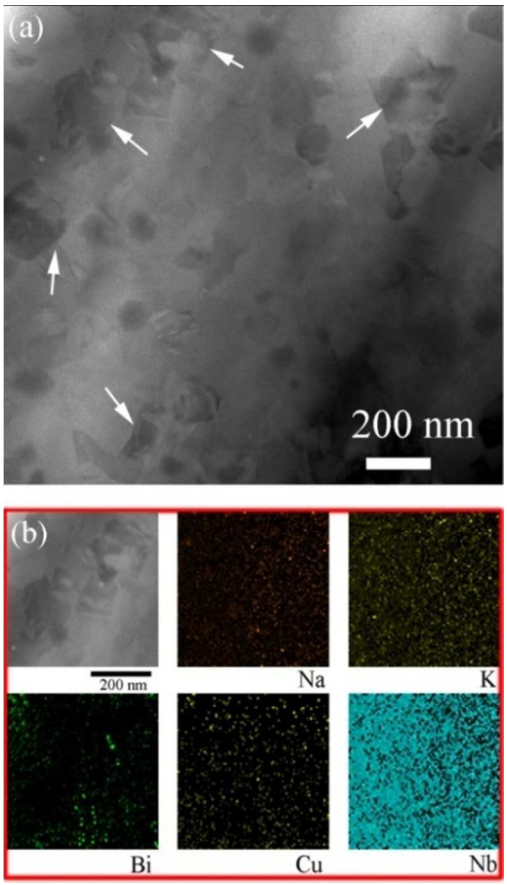

Fig. 9 (a) TEM-HAADF image of KNN-0.015BC ceramic (arrows point out the core–shell microstructures) and (b) corresponding Na, K, Bi, Cu, and Nb EDS elemental maps.

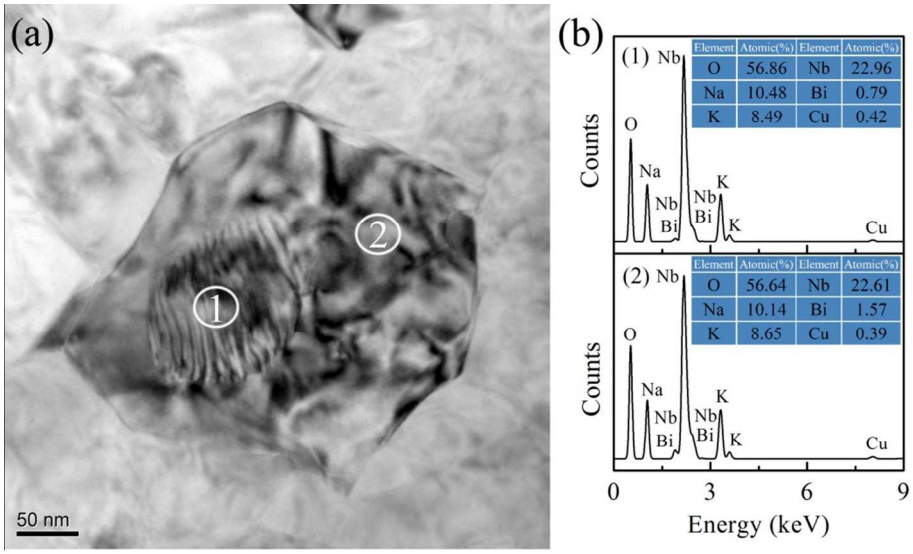

Fig. 10 Bright field TEM image and EDS chart for KNN-0.015BC ceramics.

The different dielectric characteristics in grain and grain boundary suggest that the microstructure of KNN-0.015BC ceramic is inhomogeneity. A contrast variation between the core and outer shell regions are frequency observed in TEM-HAADF image of KNN-0.015BC ceramic (Fig. 9a). TEM-HAADF imaging has the benefit that contrast is approximately proportional to atomic number squared (Z^2), and largely excludes diffraction effects.[37] It is commonly applied for imaging chemical segregation, and especially useful for providing information on core-shell grain structures.[38] Fig. 9b displays EDS elemental maps of KNN-0.015BC ceramic, the core-shell microstructure is associated with an enrichment of Bi element in the outer shell regions when compared to the grain cores. Same core-shell microstructure also can be found in KNN-0.02BC ceramic (ESI Fig. S3†).

Bright field TEM image of one grain of KNN-0.015BC ceramic was chosen to investigate, a clear core-shell structure shown in Fig. 10a. The EDS was performed within the core and shell, as illustrated in Fig. 10b. Obviously, the elements within the ceramic can be detective in the whole grain, and the elements almost homogeneously distributed except Bi. For the core region, the atomic percentage of Bi is 0.79, whereas the value is 1.57 in the shell region. The different between the core-shell grain phase compositions was so slight, thus it is hard to distinguish the second phase in XRD patterns (Fig. 1a). Such micro-heterogeneity grain gives rise to the temperature stability of permittivity. Similar situations also happen to $BiScO_3$–modified $K_{0.5}Na_{0.5}NbO_3$–$LiTaO_3$[37] and $BaTiO_3$–$Bi(Mg_{1/2}Ti_{1/2})O_3$[39] ceramics.

Conclusions

KNN–*x*BC ceramics with perovskite phase have been synthesized using the conventional solid-state sintering method. Bi and Cu co-doping have an evident effect on the grain size reduction and phase transitions temperatures decrease in the KNN–*x*BC ceramics. KNN–0.015BC ceramic shows a stable permittivity near 1350 and dielectric loss lower than 5% at a broad temperature usage range (40 °C–430 °C). In addition, the capacitance variation ($\Delta\varepsilon'/\varepsilon'_{150°C}$) is maintained smaller than ±15% around 40 °C–520 °C temperature range. Microstructure elements distribution was studied using TEM-HAADF and EDS maps. The Bi element exhibited an inhomogeneous distribution from the grain boundary to the interior. Such core-shell grain microstructure gave rise to the temperature stability of permittivity. These results confirmed that the KNN–*x*BC ceramics could be regarded as an excellent promising candidate for preparing high temperature ceramics capacitors.

Acknowledgements

This work was supported by the National Natural Science Foundation (51172187), the SPDRF (20116102130002, 20116102120016) and 111 Program (B08040) of MOE, and Xi'an Science and Technology Foundation (CX12174, XBCL-1-08), and Shaanxi Province Science Foundation (2013KW12-02), and and the SKLP Foundation (KP201421), and the Fundamental Research Funds for the Central Universities (3102014JGY01004) of China.

Notes and references

State Key Laboratory of Solidification Processing, School of Materials Science and Engineering, Northwestern Polytechnical University, Xi'an 710072, PR China Fax: 29 8849 2642; Tel.: + 86 29 88494463.
E-mail: hqfan3@163.com, and zyliumail@163.com.

† Electronic Supplementary Information (ESI) available: [details of any supplementary information available should be included here]. See DOI: 10.1039/b000000x/

1 A. Nishino, *J. Power Sources*, 1996, **60**, 137.
2 N. Raengthon, T. Sebastian, D. Cumming, I. M. Reaney and D. P. Cann, *J. Am. Ceram. Soc*., 2012, **95**(11), 3554.
3 A. Zeb, Y. Bai, T. Button and S. J. Milne, *J. Am. Ceram. Soc*., 2014, **97**(8), 2479.
4 S. Wang and G. O. Dayton, *J. Am. Ceram. Soc.*, 1999, **82**(10), 2677.
5 G. Yao, X. Wang, T. Sun and L. Li, *J. Am. Ceram. Soc.*, 2011, **94**(11), 3856.
6 G. Yao, X. Wang, Y. Zhang, Z. Shen and L. Li, *J. Am. Ceram. Soc*., 2012, **95**(11), 3525.
7 A. Zeb and S. J. Milne, *J. Eur. Ceram. Soc.*, 2014, **34**, 3159.
8 A. Zeb and S. J. Milne, *J. Eur. Ceram. Soc.*, 2014, **34**, 1727.
9 R. Dittmer, E. Anton, W. Jo, H. Simons, J. E. Daniels, M. Hoffman, J. Pokorny, I. M. Reaney and J. Rödel, *J. Am. Ceram. Soc.,* 2012, **95**(11) 3519.
10 R. Dittmer, W. Jo, D. Damjanovic and J. Rödel, *J. Appl. Phys*., 2011, **109**, 034107.
11 M. Acosta, J. Zang, W. Jo and J. Rödel, *J. Eur. Ceram. Soc.*, 2012, **32**, 4327.
12 X. Chen, Y. Wang, J. Chen, H. Zhou, L. Fang and L. Liu, *J. Am. Ceram. Soc*., 2013, **96**(11), 3489.
13 H. Cheng, H. Du, W. Zhou, D. Zhu, F. Luo and B. Xu, *J. Am. Ceram. Soc*., 2013, **96**(3), 833.
14 T. A. Skidmore, T. P. Comyn and S. J. Milne, *J. Am. Ceram. Soc*., 2010, **93**(3), 624.
15 T. Zheng, J. Wu, X. Cheng, X. Wang, B. Zhang, D. Xiao, J. Zhu, X. Wang and X. Lou, *J. Mater. Chem. C*, 2014, **2**, 8796.
16 L. Cheng, K. Wang, Q. Yu and J. Li, *J. Mater. Chem. C,* 2014, **2**, 1519.
17 L. Ramajo, M. Castro, A. Campo, J. F. Fernandez and F. Rubio-Marcos, *J. Mater. Chem. C*, 2015, **3**, 4168.
18 Z. Liu, H. Fan and C. Long, *J. Mater. Sci*., 2014, **49**, 8107.

19 L. Cheng, K. Wang, J. Li, Y. Liu and J. Li, *J. Mater. Chem. C*, 2014, **2**, 9091.
20 F. Zhu, T. A. Skidmore, A. J. Bell, T. P. Comyn, C. W. James, M. Ward and S. J. Milne, *Mater. Chem. Phys*., 2011, **129**, 411.
21 F. Azough, M. Wegrzyn, R. Freer, S. Sharma and D. Hall, *J. Eur. Ceram. Soc.*, 2011, **31**, 569.
22 X. Tan, H. Fan, S. Ke, L. Zhou, Y. Mai and H. Huang, *Mater. Res. Bull*., 2012, **47**, 4472.
23 R. Zuo, X. Fang and C. Ye, *Appl. Phys. Lett.*, 2007, **90**, 092904.
24 H. Du, W. Zhou, F. Luo, D. Zhu, S. Qu, Y. Li and Z. Pei, *J. Appl. Phys*., 2008, **104**, 044104.
25 C. Long, H. Fan and M. Li, *Dalton Trans*., 2013, **42**, 3561.
26 K. Kakimoto, K. Akao, Y. Guo and H Ohsato, *Jpn. J. Appl. Phys*., 2005, **44**, 7064.
27 J. Jehng and I. E. Wachs, *Chem. Mater*., 1991, **3**, 100.
28 Z. Wang, H. Gu, Y. Hu, K. Yang, M. Hu, D. Zhou and J. Guan, *CrystEngComm*, 2010, **12**, 3157.
29 A. Zeb and S. J. Milne, *J. Am. Ceram. Soc*., 2013, **96**(9), 2887.
30 G. Yao, X. Wang, Y. Wu and L. Li, *J. Am. Ceram. Soc.*, 2012, **95**(2), 614.
31 N. J. Kidner, N. H. Perry and T. O. Masonw, *J. Am. Ceram. Soc*., 2008, **91**(6), 1733.
32 P. Ren, N. Maso, Y. Liu, L. Ma, H. Fan and A. R. West, *J. Mater. Chem. C*, 2013, **1**, 2426.
33 J. T. S. Irvine, D. C. Sinclair and A. R. West. *Adv. Mater*., 1990, **2**, 0935.
34 M. Li, D. C. Sinclair and A. R. West, *J. Appl. Phys*., 2011, **109**, 084106.
35 M. Li and D. C. Sinclair, *J. Appl. Phys*., 2012, **111**, 054106.
36 D. C. Sinclair and A. R. West, *J. Appl. Phys*., 1989, **66**, 3850.
37 F. Zhu, M. B. Ward, J. Li and S. J. Milne, *Acta Mater*., 2015, **90**, 204.
38 F. Zhu, M. B. Ward, T. P. Comyn, A. J. Bell and S. J. Milne, *IEEE T. Ultrason. Ferr.*, 2011, **58**(9), 1811.
39 B. Xiong, H. Hao, S. Zhang, H. Liu and M. Cao, *J. Am. Ceram. Soc*., 2011, **94**(10), 3412.

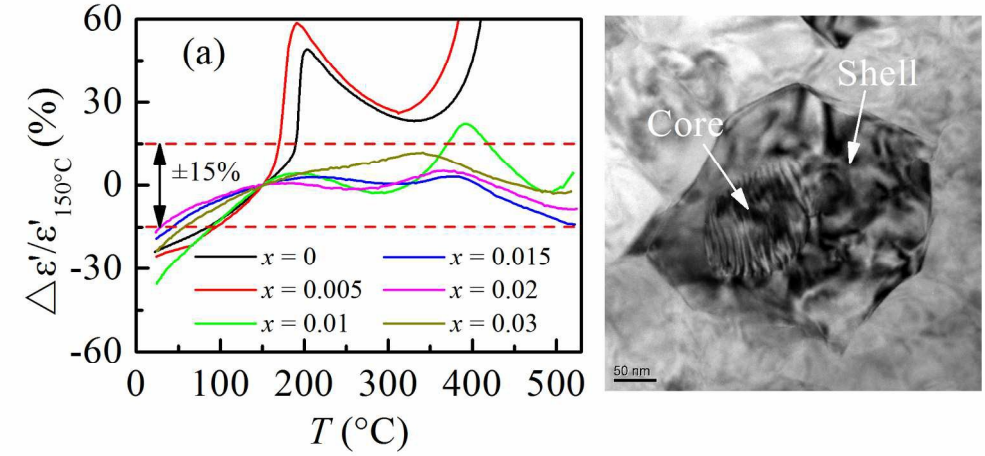

180x89mm (300 x 300 DPI)